Published in final edited form as:
J Phys D Appl Phys. 2008 ; 41(18): 185501–. doi:10.1088/0022-3727/41/18/185501.

Thermal Analysis of Gold Nanorods Heated with Femtosecond Laser Pulses

O. Ekici[*], **R. K. Harrison**[*], **N. J. Durr**[^], **D. S. Eversole**[^], **M. Lee**[*], and **A. Ben-Yakar**[*,^,°]

[*] The University of Texas at Austin, Department of Mechanical Engineering

[^] The University of Texas at Austin, Department of Biomedical Engineering

Abstract

We present an axisymmetric computational model to study the heating processes of gold nanoparticles, specifically nanorods, in aqueous medium by femtosecond laser pulses. We use a two-temperature model for the particle, a heat diffusion equation for the surrounding water to describe the heat transfer processes occurring in the system, and a thermal interface conductance to describe the coupling efficiency at the particle/water interface. We investigate the characteristic time scales of various fundamental processes, including lattice heating and thermal equilibration at the particle/surroundings interface, the effects of multiple laser pulses, and the influence of nanorod orientation relative to the beam polarization on energy absorption. Our results indicate that the thermal equilibration at the particle/water interface takes approximately 500 ps, while the electron-lattice coupling is achieved at approximately 50 ps when a 48×14 nm gold nanorod is heated to a maximum temperature of 1270 K with the application of a laser pulse having 4.70 J/m^2 average fluence. Irradiation by multiple pulses arriving at 12.5 ns time intervals (80 MHz repetition rate) causes a temperature increase of no more than 3 degrees during the first few pulses with no substantial changes during the subsequent pulses. We also analyze the degree of the nanorods' heating as a function of their orientation with respect to the polarization of the incident light. Lastly, it is shown that the temperature change of a nanorod can be modeled using its volume equivalent sphere for femtosecond laser heating within 5–15% accuracy.

Introduction

In recent years, researchers have exploited the unique optical properties of gold nanoparticles for a wide range of diagnostic and therapeutic biomedical applications. The conduction electrons of gold nanoparticles can be resonantly excited at their plasmonic frequencies in the visible and near-infrared (NIR) wavelengths. These coherent oscillations result in intense scattering and absorption of light, leading to large enhancements of the electromagnetic field near the particles [1]. These properties are directly related to the size and shape of the gold nanoparticles, which can be now synthesized in highly monodispersed solutions [2]. Furthermore, the conjugation of gold nanoparticles to probe molecules such as antibodies or aptamers has been thoroughly developed over the last several decades, allowing for convenient and reliable and molecularly specific targeting [3, 4]. Lastly, gold nanoparticles have been shown to be relatively biologically compatible at low concentrations, exhibiting low or negligible cytotoxicity [5].

The potential of gold nanoparticles as optical contrast agents for targeted imaging and therapy has been demonstrated in diagnostics [6–8], bioanalytical chemistry [9–11], and several therapeutic modalities [12, 13]. With recent developments in gold nanoparticle

[°]Corresponding author: ben-yakar@mail.utexas.edu.

synthesis, the optical properties of a variety of new asymmetrical geometries have been investigated. Gold nanorods have attracted growing interest because of their especially intense interaction with NIR light [14–16]. Gold nanorods exhibit resonance peaks at two wavelengths, corresponding to their transverse and longitudinal modes. In general, the plasmon bandwidth of gold nanorods is narrower than other particle geometries, owing to their reduced plasmon damping [17]. Additionally, it has been shown that nanorods provide greater enhancements than their spherical counterparts at comparable resonance frequencies and volumes [18, 19]. As such, gold nanorods have been applied to improve applications previously demonstrated with gold nanospheres, such as optical coherence tomography [20], photoacoustic imaging [21], two-photon luminescence imaging [22], and optical therapy [13]. Many of these applications utilize femto- and nanosecond laser pulses.

With the increasing interest in the use of nanoparticles, several levels of heat transfer modeling have been developed in support of experimental studies. Though these models have helped to gain a better understanding of the thermal processes involved in laser heating of nanoparticles, mainly spherical particles, there is still a need for an accurate model describing the heating of gold nanorods with short laser pulses.

Several groups investigated the heating of gold micro- and nanospheres with nanosecond laser pulses for selective cellular membrane poration [23–26]. Pitsillides et al. [24], for example, used time-resolved microscopy to measure the effects of nanosecond laser pulse heating of particles on cell lethality, cell membrane permeability, and protein inactivation. They used a simple heat diffusion model assuming equal temperatures at the interface and estimated the induced temperatures to gain more insight into the physics of particle/laser interaction such as heat loss during the laser pulse, the duration of peak particle temperature, and the thickness of heated fluid layer. It was concluded that selective cell damage could be achieved without affecting neighboring cells.

Hartland and co-workers examined the rate of energy dissipation from spherical gold nanoparticles heated by femtosecond laser pulses to their surroundings by time-resolved spectroscopy [27–29]. The period of the breathing modes has been measured for different sizes of particles and the corresponding temperatures are calculated using the temperature dependent elastic constants of gold. The experimental results were supported by a thermodynamic model [27, 28] which calculates the particle temperature using the heat capacity and enthalpy of fusion of gold. In another study, they calculated the relaxation time scales of cooling by solving heat transfer equations [29]. They found that the calculated times are consistently faster than the experimental results, which is mainly attributed to the equal particle and water temperature assumption at the interface.

In a recent study, Volkov et al. [30] presented a computational model for laser heating of spherical nanoparticles. The presented model solves the one-dimesional Navier-Stokes equations and includes a realistic equation of state for surrounding water to study the evolution of the pressure and temperature distribution and to approximate the bubble formation around the particle. Different models were simulated and compared against each other and it was concluded that one-temperature model for particle heating and the simplified Stiffened gas equation of state for surrounding water are inappropriate. It is worth noting that the temperatures of the particle and the surrounding water are assumed equal at their interface. However it is known that the thermal interface conductance, i.e., the temperature jump at the interface between the particle and its surroundings, plays an important role when investigating the heat transfer on the time scales of interest.

The interface conductance has been extensively discussed by Cahill and coworkers [31, 32]. A heat transfer model for the cooling process of spherical nanoparticles was presented and

solved numerically to determine the thermal interface conductance values for particles in aqueous medium by measuring the particle temperatures through time-resolved changes in optical absorption. Similarly, the thermal interface conductance has been employed in the heat transfer model presented by Plech and co-workers [33, 34] where they investigate the lattice dynamics of spherical gold nanoparticles in water medium by x-ray scattering. The model predictions are found to be in agreement with experimental results at low fluences. It has been shown that increasing fluences result in high water temperatures at the particle surface, and the heat transfer model is no longer valid when the water temperature rises to values near the critical temperature.

In this paper, we will present an axisymmetric computational model to investigate heating of gold nanorods in a water medium by single and multiple femtosecond pulses of 80 MHz repetition rate. The interaction of laser pulses with particles might result in variety of different physical processes such as shape and structure change due to melting, ablation, and fragmentation. The strength of this interaction depends on the particle size, geometry, and optical parameters. The focus of this paper will be on the heat transfer processes occurring in the system during and after the laser pulses, though before the onset of particle melting or bubble formation around the particle. The prediction of the temporal temperature profiles will be presented by taking into account the electron-phonon relaxation time for the particle, the interface conductance between the particle and its surroundings, and the diffusion dominated heat transfer within the surrounding medium. We also show the effects of nanorod orientation relative to the beam polarization on absorption efficiency and subsequent heat transfer processes. In addition, we present results to show the differences between using an axisymmetric model for an accurate description of the nanorod geometry and using a spherical model, in which the later offers an easier and faster solution. A better understanding of the interaction of gold nanorods with pulsed laser light will help further their use as contrast agents for imaging while avoiding damage to particles and tissue, as well as in therapeutic applications, where controlled destruction of cells is desirable.

Theory and Modeling

Figure 1 summarizes various processes associated during ultrafast laser heating of metal nanoparticles [35, 36]. When the particle is exposed to an ultrafast laser pulse, free electrons absorb the energy of photons, which increases their kinetic energy. These highly energetic electrons, having initially a nonequilibrium distribution of energy, are relaxed through electron-electron scattering on the order of 10–50 fs. Practically, there is no energy exchange occurring between electrons and phonons within these time scales and electrons stay in high energy levels. The particle (lattice) temperature starts increasing as a result of electron-phonon scattering. A thermal equilibrium between the electrons and lattice is reached between 10–50 ps depending on the initial rise in electron temperature. As the particle temperature increases, energy exchange between the particle and its surrounding medium begins to take place through phonon-phonon coupling. The temperature jump at the interface of the particle and the aqueous solution diminishes as a thermal equilibrium is achieved within 100 ps to 1 ns, depending on the particle size and the laser pulse intensity.

We model the heating of a single gold nanorod (48 × 14 nm) in water medium irradiated by 250 fs long laser pulses at its peak plasmonic frequency centered at 760 nm. These conditions are representative of common parameters used in two-photon luminescence imaging of nanorod labeled cancer cells [37]. Modeling laser heating of a single nanorod surrounded by a water medium is a first step towards understanding the thermal processes of nanorod heating in relation to possible imaging parameters. For imaging purposes, as a worst-case scenario for nanorod packing, we can assume 10^5 gold nanorods conjugated to the epidermal growth factor receptors (EGFR) of each cell. With an average cellular surface

area of 300 μm^2 and gold nanorod cross-sectional area of 630 nm^2, we estimate nanorods could occupy a maximum of 21% of the cell surface area. In this case, all the nanorods are aligned along the cell membrane. As such, more accurate studies should include the possible clustering effects of nanorods due to EGFR movement along the cellular membrane.

At the fluences considered in this study, heating contributions due to direct linear and nonlinear absorption of photons by water can be neglected. At pulse fluences of 5 J/m^2, using the linear absorption coefficient of water at 760 nm of $\mu_a = 2.5\ m^{-1}$ [38], the energy absorbed is 12.5 $\mu J/cm^3$ per pulse. Using a first order model, water temperature increase is equal to the energy absorbed divided by the product of the density and specific heat of water. This estimate indicates that the temperature increase is less than 10^{-6} degrees Celsius at the focal point. Furthermore, our peak irradiance is 2 GW/cm^2 (5 J/m^2 fluence divided by 250 fs pulse duration), which is approximately two orders of magnitude below the threshold of 260 GW/cm^2 necessary to create a single free electron during the pulse duration as estimated by Vogel *et al.* [39]. However, our calculations show strong enhancement.of the electromagnetic fields in the near-field of the nanorods. This enhanced region could lead to near-field ablation effects that need to be considered for a complete treatment of laser heating of nanoparticles and their surrounding water: (1) modification of nanorod geometry through near-field ablation [40, 41] and/or (2) free electron generation in water leading to its additional heating and thus creation of bubbles at lower laser fluences [34, 39]. These effects will be considered in future studies.

The equations describing the transient temperature response of the gold nanorod in a water medium under the influence of laser radiation are given by Eqns. (1) and (2). Since the conduction electrons in the gold nanorod absorb the laser pulse energy, the two-temperature model (TTM) is used to describe the laser absorption and the subsequent electron-phonon equilibration in the particle [42].

$$C_e \frac{dT_e}{dt} = g(T_l - T_e) + \frac{E_{abs}}{V_p \cdot \tau_{pulse}} \tag{1}$$

$$C_l \frac{dT_l}{dt} = g(T_e - T_l) - \frac{\dot{Q}_w}{V_p} \quad if \quad (T_l < T_m). \tag{2}$$

Here V_p is the volume of the particle, τ_{pulse} is the laser pulse width, T_e and T_l are the electron and lattice temperatures of the particle, E_{abs} is the laser pulse energy absorbed by the particle, g is the coupling factor to calculate the heat transfer rate from electrons to the lattice, $\dot{Q}_w$ is the rate of heat loss from particle to its surroundings, C_e and C_l are the heat capacities for electrons and the lattice of bulk gold, respectively. Table 1 summarizes the specific values of the thermophysical properties used in this paper.

The laser energy absorbed by the particle depends on the laser fluence, F_{pulse}, and the absorption cross-sectional area of the nanorod, A_{abs}, according to

$$E_{abs} = A_{abs} \cdot F_{pulse}. \tag{3}$$

When noble-metal nanoparticles are exposed to light at their plasmonic frequency, the effective absorption cross section will be much larger than the geometrical one. *Aabs* was

calculated using the "efficient" ADDA code package according to the discrete dipole approximation method which has been extensively reviewed in the literature [43–45]. The nanorods were modeled as spherically capped cylinders and consisted of approximately 5 million dipoles. The large number of dipoles per wavelength was used to reduce the error due to the large indices of refraction of gold at these wavelengths [46]. The water environment surrounding the nanoparticles was assumed to have a uniform index of refraction of 1.333. Dielectric constants for the nanoparticles were obtained from Palik [47] and the values were corrected for the size-induced damping with the volume-equivalent effective radius and the method and constants used in Scaffardi and Tocho [48]. Table 2 summarizes the key parameters used in the calculations of effective cross-sectional area for the nanoparticles considered in this paper.

The rate of heat loss from the particle to its surroundings in Eq. (2) is calculated by taking into account the interface conductance given by

$$\dot{Q}_w = A_{surface} \cdot \mathrm{G} \cdot (T_l - T_{w,s}) \tag{4}$$

where $T_{w,s}$ is the water temperature at the particle surface, G is the thermal conductance at the particle/fluid interface, and $A_{surface}$ is the surface area of the particle. The thermal conductance G relates the temperature drop at an interface to the heat flux crossing the interface and constitutes the coupling parameter between a particle and surrounding medium energy equations.

The particle geometry, a cylindrical nanorod, allows us to use an axisymmetric model to describe the energy transfer within the surrounding medium. Therefore, the energy conservation equation for water can be written in cylindrical coordinates as:

$$\rho_w c_{p,w} \frac{\partial T_w}{\partial t} = \frac{\partial}{\partial z}\left(k \frac{\partial T_w}{\partial z}\right) + \frac{1}{r}\frac{\partial}{\partial r}\left(kr \frac{\partial T_w}{\partial r}\right). \tag{5}$$

As can be seen from the above equations, uniform temperatures are assumed across the particle. This assumption is quite appropriate considering the characteristic length scales of the problem. The calculated Biot number, $Bi = \mathrm{G} \cdot L_c / k_{\mathrm{gold}}$, is on the order of 10^{-3}. The characteristic length, L_c, is defined as the volume of the particle divided by the surface area of the particle and k_{gold} is the thermal conductivity of bulk gold. Typically the lumped capacitance model of transient heat transfer introduces less than 5% error for Biot numbers smaller than 0.1.

In the simulations, we use a pulse wave to characterize the temporal profile of a laser pulse. It is worth to note that the choice of temporal profile has no considerable effect on lattice temperature in the case of femtosecond laser irradiation because the electron-phonon coupling time, on the order of tens of ps, is much larger than the pulse duration.

The model and equations presented are valid in the absence of phase changes and therefore we need to observe two temperature limits. The first limit is the melting temperature of gold nanorod (T_m~1337 K) since the rod-to-sphere shape change due to melting is not included in the model. The second limit is the critical temperature of water (T_{cr}=647 K) since explosive boiling is not included.

In the first limit, the particle temperature, T_l, rises until it reaches the melting point of gold, and then it remains constant during the phase change. Once the melting temperature is

reached, any additional energy contributes to the phase change, which can be calculated using

$$\Delta E = \int_{\Delta t} (V_p \cdot g(T_e - T_l) - \dot{Q}_w) \cdot dt \quad if \quad (T_l = T_m). \tag{6}$$

On the other hand, the energy required for complete melting after the particle reaches the melting temperature depends on the heat of fusion of gold, ΔH_{fus};

$$E_{phase-change} = \rho_{gold} \cdot V_p \cdot \Delta H_{fus}. \tag{7}$$

The complete melting of the particle is achieved when $\Delta E = E_{phase\text{-}change}$ and at this point the particle temperature starts increasing again beyond its melting value.

In the second limit, when close to the critical temperature, the water becomes thermodynamically unstable (i.e., an upper limit for superheating) and a vapor layer is formed around the particle which would, in turn, change the heat transfer at the surface drastically. In principle, the phase change can occur at any point between the binodal (equilibrium vaporization, normal boiling) and spinodal (superheating limit) lines depending on the vapor pressure. In the case of high rates of energy deposition, such as femtosecond laser pulse irradiation, the pressure build-up occurs at a slower rate when compared with the temperature rise; as such, superheating is observed instead of phase change [30, 34, 54, 55]. The spinodal line forms an upper limit for the superheated liquid and when it is reached, an explosive phase change (boiling) occurs. A significant amount of vapor nuclei can be found when the temperature of the liquid reaches 90% of the critical temperature [34, 54, 56, 57].

Numerical Solution

Figure 2 shows the computational domain. Because of the symmetry of the computational domain with respect to the r- and z- axes, only one quarter of the axisymmetric geometry is modeled. Discretization of the computational domain is made by non-uniformly distributed grids which are generated in accordance with particle geometry. In the simulations, we used a minimum length for the grid edge of 0.25 nm and time-steps of 2.5 fs and 25 fs for particle and water temperature calculations, respectively. These numerical parameters are determined by verifying that further refining the grid and decreasing the time-step do not cause any appreciable changes in the simulation results.

Equations (1) and (2) for the lattice and electron temperatures, respectively, are numerically solved using the modified Euler method. The energy equation for the surrounding water, Eq. (5), is discretized through the finite volume formulation and solved implicitly by the time-splitting technique to get second order accuracy in time and space.

Initial and boundary conditions

The transient simulations presented in this study use the ambient temperature value of 300 K as an initial condition. Neumann boundary condition is used for the surrounding water and set to zero at the boundaries of the computational domain. The thermal conduction G is used at the particle/water interface as explained earlier in the text.

Model validation

The lattice expansion measurements of spherical gold nanoparticles in water by Kotaidis et al. [34] are used to validate the theoretical model and the computational tool developed for this study. The effective area calculations for spheres were performed using a Mie theory code derived from the equations given in Bohren and Huffman [52]. We have used the calculated lattice temperature to predict the thermal expansion by:

$$\frac{\Delta a}{a}=\alpha_{\text{gold}}(T)\cdot\Delta T, \tag{8}$$

where the linear thermal expansion coefficient of gold is: $\alpha_{\text{gold}}(T)\times10^{6} = 12.00269 + 0.00953\cdot T - 8.4\cdot10^{-6}\cdot T^{2} + 5.43\cdot10^{-9}\cdot T^{3}$. [53]

Figure 3 shows the calculated values of the lattice expansion measurements of 52 nm and 94 nm gold particles at 100 ps and 1 ns after irradiation by a 400 nm, 100 fs laser pulse along with data provided by Kotaidis et al. [34] as a function of laser fluence. The agreement between the experimental data and the model predictions is quite satisfactory especially for the low fluence values where the measured lattice expansion increases linearly with the applied fluence for both particle sizes. It is seen that the nonlinear changes, which cannot be predicted with the presented model, are observed at earlier fluence values for the measurements with 1 ns delay compared to those with 100 ps delay. As has been discussed in detail by Kotaidis et al. [34], the mismatch at relatively high fluences can be attributed to the breakdown of the assumptions made in the heat transfer model due to high temperatures (close to the critical value) of surrounding water. Therefore, it is concluded that the model and the solver employed in this study can be used to describe the heat transfer processes for the nanoparticles as long as the model assumptions are not violated.

Results and discussion

We first discuss the heating of a single gold nanorod and its surrounding exposed to a single femtosecond laser pulse with a nominal fluence value of 4.70 J/m^2. This particular fluence value is chosen to avoid reaching two critical temperature limits: the melting temperature of gold and the critical temperature of water, in order to stay within the assumptions of the model used in this study. As will be seen hereafter in the presented results, the simulation with the base fluence value of 4.70 J/m^2 predicts a maximum temperature of approximately 1270 K for the particle and of around 580 K for the surrounding water temperature at the particle surface. At these values, the particle temperature is lower than the bulk melting temperature of gold and the surrounding water temperature is lower than 90% of the critical temperature for water.

Figure 4 shows temperature contours at 70 ps after irradiation with an average laser fluence of 4.70 J/m^2, at which point the water temperature reaches its maximum value. At 70 ps, the water temperature reaches about 580 K at the mid-length of the nanorod (z = 0). At the same time, the particle temperature is 1079 K after dropping from its maximum value of 1270 K achieved at 30 ps after the laser pulse. High water temperatures at the interface decrease rapidly as we move away from the particle in any direction where the thermal penetration depth (defined by the length where temperature drops to around 300 K) is approximately 7 nm.

Figure 5 presents the temperature profiles as a function of radial distance at different times in the z=0 plane. The plot shows that initially, there is a large temperature jump at the particle/water interface decreasing with time, and becoming negligible at about 500 ps after

the laser pulse. The thermal penetration depth, about 7 nm at 50 ps, increases to 20 nm at 500 ps after the pulse when the particle temperature drops to around 400 K.

Figure 6 shows the electron and lattice temperatures of the particle and the water temperature near the particle surface as a function of time after irradiation with a single laser pulse. The electron temperature rises during the pulse duration (250 fs) and reaches its maximum value at the end of the pulse. This quick electron temperature rise can be seen as an instantaneous process compared with the time scales of the subsequent electron-phonon and phonon-phonon coupling processes. Thermal equilibrium between the electrons and the lattice occurs approximately 50 ps after the pulse. On the other hand, the temperature difference at the interface between the particle surface and the adjacent water becomes negligible at around 500 ps after the pulse.

We next study the effects of multiple laser shots on the temperatures of the gold nanorod and its surrounding water. Figure 7 presents transient temperature profiles for the duration of an imaging session of 1 μs, during which the nanorods are excited by 80 laser pulses arriving at 12.5 ns time intervals from an 80 MHz repetition rate laser system. Two main observations result from the calculations. First, the temperatures of the electron and lattice of the particle and the temperature of water at the particle surface equilibrate before the arrival of the next pulse. This result is rather trivial, considering the relaxation times of 50 ps and 500 ps for electron-phonon and phonon-phonon (across the particle and water interface) couplings, respectively. Second, an overall temperature rise of only 3 K is calculated during the first few pulses and thereafter no significant temperature increase is observed.

Figure 8 presents the effects of laser fluence on the maximum temperature values. The results show three distinctive regions: approximately linear temperature rise with increasing fluence, constant temperature plateau during a phase change (melting), and linear temperature rise again following the completion of melting. It is important to note that the phase change of the surrounding water was not included in this study. This approximation fails to hold especially for the fluences beyond ~4.70 J/m^2 which is the value where the water temperature at the surface reaches 90% of its critical value. Therefore, temperature estimates for fluences larger than the base fluence (4.70 J/m^2) should be approached with care and be accepted as first order approximations. Since we reach 90% of the critical water temperature before the particle melting begins, bubble formation might result in reduced heat dissipation from the particle. In this case, we might expect to observe melting of the particle at a lower fluence than the value presented here.

In the model used throughout the paper, the heat transfer from a particle to the surrounding water is taken into account and maximum temperatures for the nanoparticle lattice and water at the particle surface are calculated. As can be seen in Fig. 8 with the lattice temperature shown with a solid line, the particle reaches its melting temperature at a fluence of 5.10 J/m^2. When heat transfer from the particle to its surroundings is neglected, as assumed by some of the earlier studies [58, 59] the particle reaches the melting temperature at a lower fluence of 3.90 J/m^2. We conclude that, although the time scales of the problem are extremely short, the heat transfer between the particle and its surroundings (i.e., heat loss from the particle) should not be neglected.

Figure 8 also shows that the fluence required to melt the nanorods (48×14 nm) completely is 7.15 J/m^2, corresponding to a total absorbed energy of 36 fJ. For comparison, we also modeled the melting of nanorods studied by El-Sayed and coworkers [58, 59]. These nanorods had a mean aspect ratio of 4.1 with dimensions of 44×11 nm. With our computational model, we estimated that about 21.5 fJ is required to completely melt these nanorods using the beam parameters presented in their study. On the other hand, Link and

El-Sayed [59] determined a larger threshold energy of about 65 fJ for complete melting. They estimated this required energy by dividing the absorbed laser energy by the total number of nanorods in the sample volume. This calculation, however, neglects the dependence of energy absorption on the nanorod orientation. It is known that the effective absorption cross-section and the corresponding energy absorption of a gold nanorod depend strongly on the angle of the longitudinal axis with respect to the polarization. The absorption efficiency can range by almost 3 orders magnitude from the orientation where the polarization and the long axis of the nanorods are parallel to the minimum when the nanorods are aligned perpendicularly for the nanorods considered in this study.

To show the effects of orientation for isotropically distributed nanorods, the percentage of completely melted nanorods is plotted against the incident fluence in Fig. 9. For both sets of nanorods presented, it is observed that an increase of one order of magnitude in fluence is required to melt 65% of isotropically arranged nanorods compared with nanorods aligned perfectly parallel to the electric field polarization. The estimated average threshold fluence for melting all of the randomly oriented nanorods is experimentally determined by Link and El-Sayed [58] and found to be approximately 100 J/m^2. Their study was performed with multiple femtosecond pulses in a rotating cuvette. This fluence corresponds to a melted fraction of 75% of isotropically distributed nanorods in our computational model which is seen to be in good agreement given that the nanorods in the experiment pass through the focal volume multiple times over the course of irradiation. It is also observed that the difference between melting fluences for the two sets of nanorods presented in Fig. 9 becomes less significant as a higher percentage of nanorods are melted.

Lastly, we investigate the effects of geometry modeling on the temperature history of nanoparticle. Figure 10 shows the transient temperature profiles for two sets of nanorods and their volume equivalent spheres. We kept the absorption cross sections equal to the ones of the corresponding nanorods. We observe that the predicted temperature profiles show good agreement for both sets especially during particle heating. The errors are less than 5% during particle heating and 15% during particle cooling. Because the surface area of the nanorod is larger than its volume equivalent sphere it experiences a faster cooling to the surroundings. In addition, the discrepancy between the predicted temperatures for the nanorods and their volume equivalent spheres increases with increasing aspect ratio as a result of relative increase in surface area to volume ratio.

Conclusion

This study presents a theoretical model to simulate the heat transfer processes of a femtosecond laser irradiated cylindrical gold nanorod in water medium. We studied the characteristic time scales of the problem (i.e., electron-phonon and phonon-phonon coupling), the effects of multiple laser pulses, and orientational dependence of nanorod energy absorption.

First, we validated our model by simulating the heating of spherical particles and comparing the results with the lattice expansion measurements of Kotaidis et al. [34]. We studied 48×14 nm gold nanorod heating by a single 250 fs laser pulse. The results show that the water temperature at the surface of a particle reaches approximately 90% of its critical value at the fluence of 4.70 J/m^2 and the particle reaches its melting temperature of 1337 K at the fluence of 5.10 J/m^2 when the laser polarization and nanorod axes are parallel. It is also shown that the complete particle melting occurs at the fluence of 7.15 J/m^2.

We investigated the influences of multiple pulse irradiations on the heating of gold nanorods. It is shown that the temperatures of gold nanoparticle and water relax to room

temperature before the next pulse arrives 12.5 ns later at 80 MHz pulse repetition rate. Irradiation with multiple pulses causes an overall temperature rise of approximately 3 K during the first few pulses with no subsequent changes in the following pulses. This result is important for two-photon luminescence imaging using the gold nanoparticles. The results show that the particles will not accumulate heat during imaging and the particles will melt only during the initial laser pulses when the laser fluence is larger than the melting threshold for a single laser pulse.

In addition, we investigated the dependence of the energy absorption on the orientation of nanorods with respect to laser polarization. The melting fluence is found to increase by almost 3 orders of magnitude from nanorods aligned with the polarization to those that are aligned perpendicularly. Melting 65% of isotropically distributed nanorods in a volume would require an order of magnitude larger fluence than the one necessary to melt a single, aligned nanorod. Finally, we also showed that ultrafast heating of gold nanorods can be described with a spherical model within 5–15% of accuracy.

As previously noted, recently, there has been much interest in the use of gold nanoparticles in biomedical applications. Simulations such as the one presented here will be an integral part of the research in this emerging field to help investigating the physical processes. In our future research, we will solve the full set of compressible equations with a model allowing the phase change of surrounding water and examine the effects of pressure and bubble formation around the particle.

Acknowledgments

We thank Dr. Anton Plech for providing the experimental data for the lattice expansion measurements of spherical gold nanoparticles presented in Figure 3. This work was supported by the National Institutes of Health grant RO3 CA125774 and by the Texas Higher Education Coordinating Board through Advanced Research Program (ARP) grant.

References

1. Kreibig, U.; Vollmer, M. Optical Properties of Metal Clusters. Springer; Germany: 1995.
2. Frens G. Controlled nucleation for the regulation of particle size in monodisperse gold solutions. Nature Physical Science. 1973; 20:241.
3. Horisberger M. Colloidal gold: a cytochemical marker for light and fluorescent microscopy and for transmission and scanning electron microscopy. Scanning electron microscopy. 1981; 2:9–31. [PubMed: 7034182]
4. Goodman SL, Hodges GM, Livingston DC. A review of the colloidal gold marker system. Scanning electron microscopy. 1980; 2:133–46. [PubMed: 6999596]
5. Lewinski N, Colvin V, Drezek R. Cytotoxicity of nanoparticles. Small. 2008; 4:26–49. [PubMed: 18165959]
6. Schultz S, Smith DR, Mock JJ, Schultz DA. Single-target molecule detection with nonbleaching multicolor optical immunolabels. Proceedings of the National Academy of Sciences. 2000; 97:996–1001.
7. Sokolov K, Follen M, Aaron J, Pavlova I, Malpica A, Lotan R, Richards-Kortum R. Real-time vital optical imaging of precancer using anti-epidermal growth factor receptor antibodies conjugated to gold nanoparticles. Cancer Research. 2003; 63:1999–2004. [PubMed: 12727808]
8. El-Sayed I, Huang X, El-Sayed M. Surface plasmon resonance scattering and absorption of anti-EGFR antibody conjugated gold nanoparticles in cancer diagnostics: Applications in oral cancer. Nano Letters. 2005; 5:829–834. [PubMed: 15884879]
9. Nie S, Emory SR. Probing single molecules and single nanoparticles by surface-enhanced Raman scattering. Science. 1997; 275:1102–1106. [PubMed: 9027306]

10. Elghanian R, Storhoff JJ, Mucic RC, Letsinger RL, Mirkin CA. Selective colorimetric detection of polynucleotides based on the distance-dependent optical properties of gold nanoparticles. Science. 1997; 277:1078–1081. [PubMed: 9262471]
11. Kneipp K, Haka AS, Kneipp H, Badizadegan K, Yoshizawa N, Boone C, Shafer-Peltier KE, Motz JT, Dasari RR, Feld MS. Surface-enhanced Raman spectroscopy in single living cells using gold nanoparticles. Applied Spectroscopy. 2002; 56:150–154.
12. Hirsch LR, Stafford RJ, Bankson JA, Sershen SR, Rivera B, Rrice RE, Hazle JD, Halas NJ, West JL. Nanoshell-mediated near-infrared thermal therapy of tumors under magnetic resonance guidance. PNAS. 2003; 23:13549–13554. [PubMed: 14597719]
13. Huang X, El-Sayed IH, Qian W, El-Sayed MA. Cancer cell imaging and photothermal therapy in the near-infrared region by using gold nanorods. J Am Chem Soc. 2006; 128:2115–2120. [PubMed: 16464114]
14. Mohamed M, Volkov V, Link S, El-Sayed MA. The 'lightning' gold nanorods: fluorescence enhancement of over a million compared to the gold metal. Chemical Physics Letters. 2000; 317:517–523.
15. Hao E, Schatz G. Electromagnetic fields around silver nanoparticles and dimers. Journal of Chemical Physics. 2004; 120:357–366. [PubMed: 15267296]
16. Hao E, Schatz G, Hupp J. Synthesis and optical properties of anisotropic metal nanoparticles. Journal of Fluorescence. 2004; 14:331–341. [PubMed: 15617376]
17. Sonnichsen C, Franzl T, Wilk T, von Plessen G, Feldmann J, Wilson O, Mulvaney P. Drastic Reduction of Plasmon Damping in Gold Nanorods. Phys Rev Lett. 2002; 88:077402. [PubMed: 11863939]
18. Hao E, Schatz G. Electromagnetic fields around silver nanoparticles and dimers. Journal of Chemical Physics. 2004; 120:357–366. [PubMed: 15267296]
19. Hao E, Schatz G, Hupp J. Synthesis and optical properties of anisotropic metal nanoparticles. Journal of Fluorescence. 2004; 14:331–341. [PubMed: 15617376]
20. Oldenburg AL, Hansen MN, Zweifel DA, Wei A, Boppart SA. Plasmon-resonant gold nanorods as low backscattering albedo contrast agents for optical coherence tomography. Optics Express. 2006; 14:6724–6738. [PubMed: 19516854]
21. Agarwal A, Huang SW, O'Donnell M, Day KC, Day M. Targeted gold nanorod contrast agent for prostate cancer detection by photoacoustic imaging. J Appl Phys. 2007; 102:064701–4.
22. Wang H, Huff TB, Zweifel DA, He W, Low PS, Wei A, Cheng J. In vitro and in vivo two-photon luminescence imaging of single gold nanorods. Proceedings of the National Academy of Sciences of the United States of America. 2005; 102:15752–15756. [PubMed: 16239346]
23. Hüttmann G, Radt B, Serbin J, Lange BI, Birngruber R. High precision cell surgery with nanoparticles? Med Laser Appl. 2002; 17:9–14.
24. Pitsillides CM, Joe EK, Wei X, Anderson RR, Lin CP. Selective cell targeting with light-absorbing microparticles and nanoparticles. Biophysical Journal. 2003; 84:4023–4032. [PubMed: 12770906]
25. Hüttmann G, Yao C, Endl E. New concepts in laser medicine: Towards a laser surgery with cellular precision. Med Laser Appl. 2005; 20:135–139.
26. Letfullin RR, Joenathan C, Georger TF, Zharov VP. Laser-induced explosion of gold nanoparticles: potential role for nanophotothermolysis of cancer. Nanomedicine. 2006; 1:473–480. [PubMed: 17716149]
27. Hartland H, Hu M. Photophysics of metal nanoparticles: heat dissipation and coherent excitation of phonon modes. Proceedings of SPIE. 2002:4807.
28. Hartland GV, Hu M, Sader JE. Softening of the symmetric breathing mode in gold particles by laser-induced heating. J Phys Chem B. 2003; 107:7472–7478.
29. Hu M, Hartland GV. Heat dissipation for Au particles in aqueous solution: relaxation time versus size. J Phys Chem B. 2002; 106:7029–7033.
30. Volkov AN, Sevilla C, Zhigilei LV. Numerical modeling of short pulse laser interaction with Au nanoparticle surrounded by water. Applied Surface Science. 2007; 253:6394–6399.
31. Wilson OM, Hu X, Cahill DG, Braun PV. Colloidal metal particles as probes of nanoscale thermal transport in fluids. Physical Review B. 2002; 66:224301.

32. Ge Z, Cahill DG, Braun PV. AuPd metal nanoparticles as probes of nanoscale thermal transport in aqueous solution. J Phys Chem B. 2004; 108:18870–18875.
33. Plech A, Kotaidis V, Grésillon S, Dahmen C, von Plessen G. Laser-induced heating and melting of gold nanoparticles studied by time-resolved x-ray scattering. Physical Review B. 2004; 70:195423.
34. Kotaidis V, Dahmen C, von Plessen G, Springer F, Plech A. Excitation of nanoscale vapor bubbles at the surface of gold nanoparticles in water. J Chem Phys. 2006; 124:184702. [PubMed: 16709126]
35. Majumdar, A. Microscale energy transport in solids. In: Tien, Chang-Lin; Majumdar, Arunava; Gerner, Frank M., editors. Microscale energy transport. Taylor & Francis; Washington, D.C: 1998.
36. Chen, G. Nanoscale energy transport and conversion. Oxford University Press; New York: 2005.
37. Durr NJ, Larson T, Smith DK, Korgel BA, Sokolov K, Ben-Yakar A. Two-photon luminescenece imaging of cancer cells using molecularly targeted gold nanorods. Nano Letters. 2007; 7(4):941–945. [PubMed: 17335272]
38. Hale GM, Querry MR. Optical constants of water in the 200nm to 200um wavelength region. Appl Opt. 1973; 12:555–563. [PubMed: 20125343]
39. Vogel A, Noack J, Hüttman G, Paltauf G. Mechanisms of femtosecond laser nanosurgery of cells and tissues. Appl Phys B. 2005; 81:1015–1047.
40. Plech A, Kotaidis J, Lorenc M, Boneberg J. Femtosecond laser near-field ablation from gold nanoparticles. Nature Phys. 2006; 2:44–47.
41. Eversole D, Luk'yanchuk B, Ben-Yakar A. Plasmonic laser nanoablation of silicon by the scattering of femtosecond pulses near gold nanospheres. Appl Phys A. 2007; 89:283–291.
42. Kaganov M, Lifshitz IM, Tanatarov LV. Relaxation between electrons and crystalline lattices. Sov Phys JETP. 1957; 4:173.
43. Purcell EM, Pennypacker CR. Scattering and absorption of light by nonspherical dielectric grains. Astrophysics Journal. 1972; 186:705–714.
44. Draine BT, Flatau PJ. Discrete-Dipole approximation for scattering calculations. Journal of the Optical Society of America A. 1994; 11:1491–1499.
45. Yurkin MA, Hoekstra AG. The discrete dipole approximation: an overview and recent developments. Journal of Quantitative Spectroscopy and Radiative Transfer. 2007; 106:558–589.
46. Ayranci I, Vaillon R, Selçuk N. Performance of discrete dipole approximation for prediction of amplitude and phase of electromagnetic scattering by particles. Journal of Quantitative Spectroscopy and Radiative Transfer. 2007; 103:83–101.
47. Lynch, DW.; Hunter, DR. In Handbook of Optical Constants of Solids. Palik, ED., editor. Academic Press; New York: 1985. p. 294
48. Scaffardi L, Tocho J. Size dependence of refractive index of gold nanoparticles. Nanotechnology. 2006; 17:1309–1315.
49. Qiu TQ, Tien CL. Heat Transfer Mechanisms during Short-Pulse Laser Heating of Metals. ASME J Heat Transfer. 1993; 115:835–841.
50. Barin, I. Thermochemical Data of Pure Substances. Vol. Part 1. VCH; New York: 1993.
51. Hohlfeld J, Wellershoff S-S, Güdde J, Conrad U, Jähnke V, Matthias E. Electron and Lattice Dynamics following Optical Excitation of Metals. Chem Phys. 2000; 251:237–258.
52. Bohren, CF.; Huffman, DR. Absorption and scattering of light by small particles. Wiley; New York: 1983.
53. Touloukian, YS.; Kirby, RK.; Taylor, RE.; Desai, PD. Thermodynamical Properties of Matter. IFI; Thermal expansion- Metallic elements and alloys in.
54. Xu X. Phase explosion and its time lag in nanosecond laser ablation. Applied Surface Science. 2002; 197–198:61–66.
55. Dou Y, Zhigilei LV, Winograd N, Garrison BJ. Explosive boiling of water films adjacent to heated surfaces: A microscopic description. J Phys Chem A. 2001; 105:2748–2755.
56. Hu M, Petrova H, Hartland GV. Investigation of gold nanoparticles in aqueous solution at extremely high lattice temperatures. Chemical Physics Letters. 2004; 391:220–225.
57. Debenedetti, PG. Metastable Liquids: Concepts and Principles. Princeton University Press; Princeton: 1996.

58. Link S, Burda C, Nikoobakht B, El-Sayed MA. Laser-induced shape changes of colloidal gold nanorods using femtosecond and nanosecond laser pulses. J Phys Chem B. 2000; 104:6152–6163.

59. Link S, El-Sayed MA. Spectroscopic determination of the melting energy of gold nanorod. J Chem Phys. 2001; 114:2362–2368.

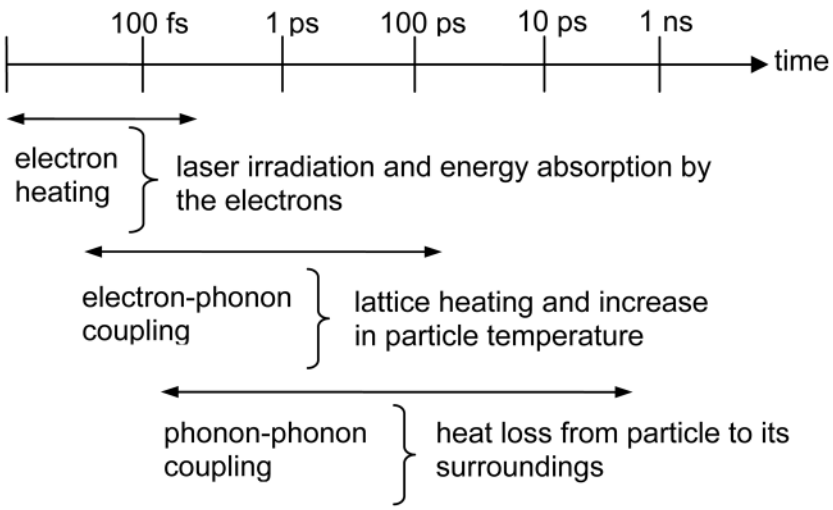

Figure 1.
Time scales of the fundamental processes in ultrafast laser heating of metal nanoparticles before the onset of particle melting or bubble formation in the surrounding aqueous solution.

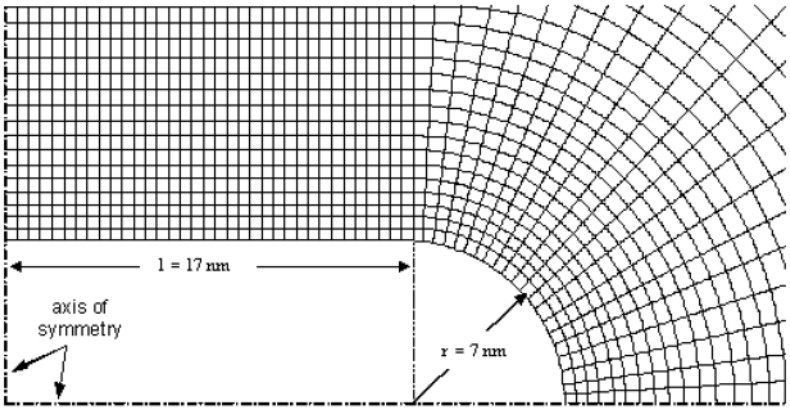

Figure 2.
Computational domain and nanorod dimensions.

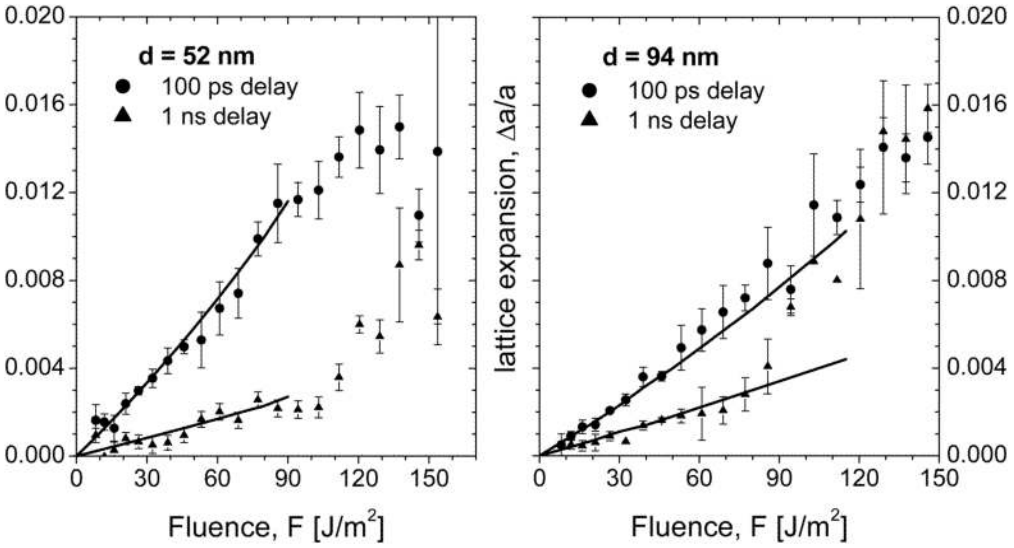

Figure 3.

Lattice expansion of spherical gold nanoparticles of 52 nm and 94 nm diameters as a function of peak laser fluence. Lines are calculated lattice expansion values up to the fluence at which 90% critical temperature of water is reached, symbols are experimental data by Kotaidis et al. [34].

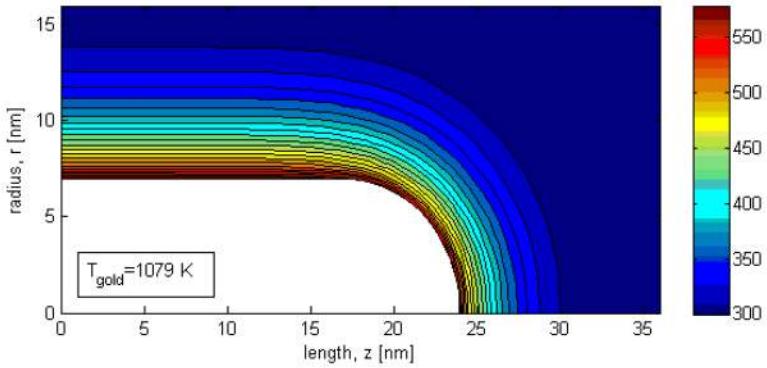

Figure 4.
Temperature distribution in water surrounding the 48×14 nm gold nanorod at 70 ps after irradiation by a 250 fs laser pulse with an average fluence of 4.70 J/m^2.

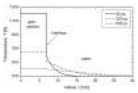

Figure 5.
Temperature profiles at different times after laser exposure (F_{pulse} = 4.70 J/m^2) as a function of radial distance in the mid-length of the 48×14 nm gold nanorod at the z=0 plane.

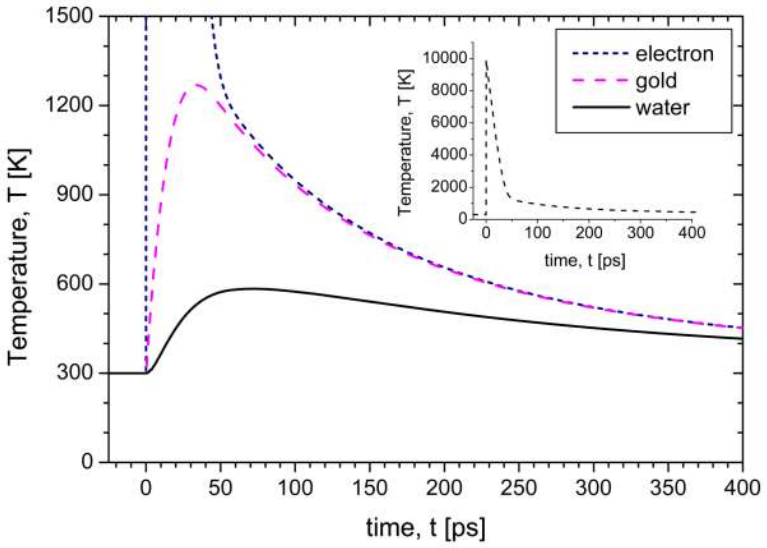

Figure 6.

Temporal evolution of temperature profiles of 48×14 nm gold nanorod and its surrounding water at the surface following irradiation with a laser pulse of fluence, F_{pulse} = 4.70 J/m^2. In the inset, the electron temperature as a function of time is shown.

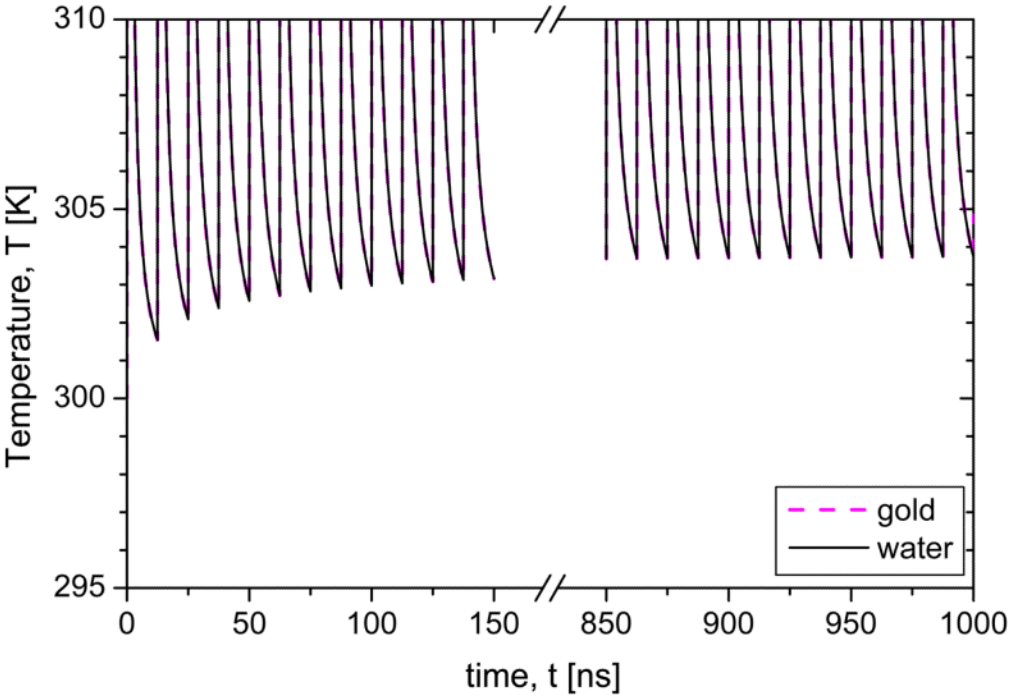

Figure 7.
Temporal evolution of temperature profiles of 48×14 nm gold nanorod and its surrounding water at the surface during a 1 μs time duration of multiple laser exposures at a repetition rate of 80 MHz with F_{pulse} = 4.70 J/m^2.

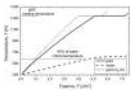

Figure 8.
Maximum temperatures of 48×14 nm gold nanorod and its surrounding water at the surface as a function of incident laser fluence, Q_w=0 represents the simulation results where the heat transfer from particle to its surrounding is neglected. Temperature estimates for fluences larger than 4.70 J/m^2 (where the 90 % of water critical temperature is reached) should be accepted as first order approximations, see the text for details.

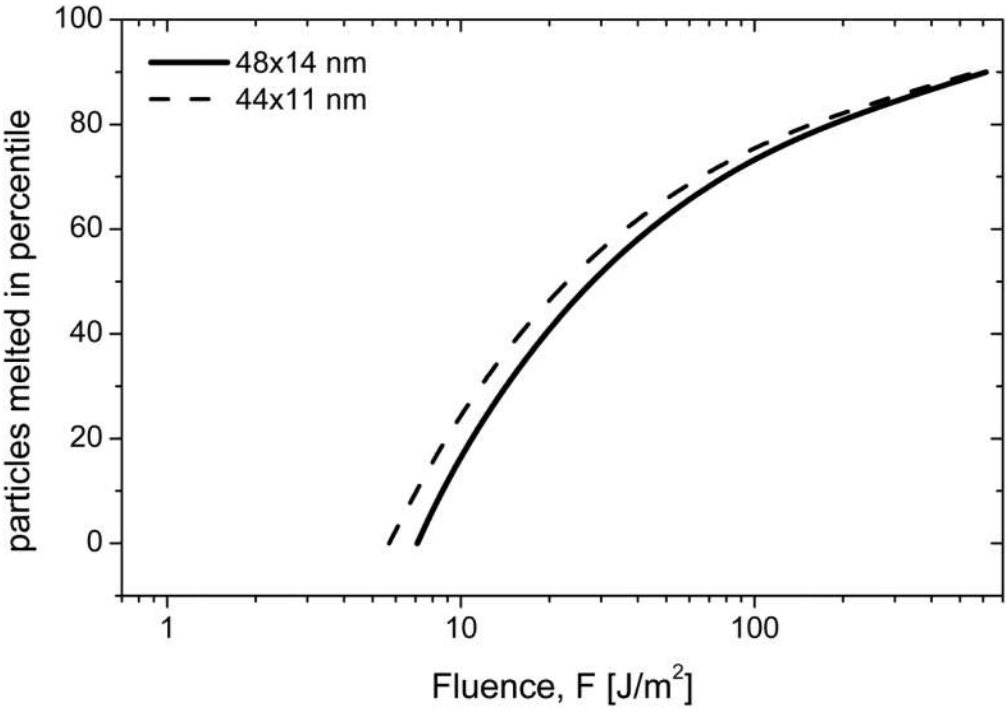

Figure 9.
Percentage of particles melted as a function of fluence assuming an isotropic distribution of nanorods in three-dimensional space.

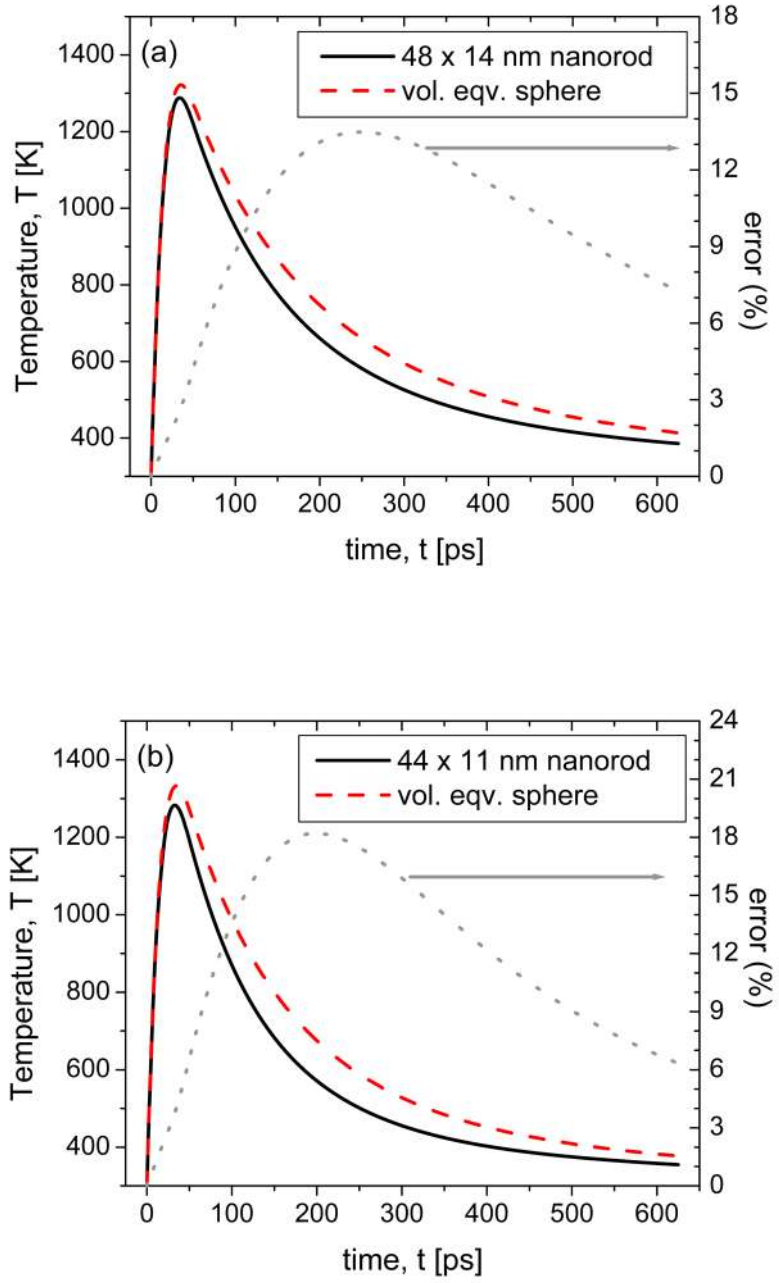

Figure 10.

Transient temperature profiles for two sets of nanorods and their volume equivalent spheres with the associated error for (a) 48×14 nm nanorod irradiated with F_{pulse} = 4.80 J/m^2 and (b) 44×11 nm nanorod irradiated with F_{pulse} = 3.80 J/m^2.

Table 1

Thermophysical properties of water and gold used in the calculations

Gold (bulk) properties	
The electron heat capacity, C_e (J/m^{3}K)	$70.0 \cdot T_e$ [49]
Specific heat of lattice, C_l (J/m^{3}K)	ρ_{gold} [$109.579T + 0.128T - 3.4 \cdot 10^{-4} T^2 + 5.24 \cdot 10^{-7} T^3$ − [50] $3.93 \cdot 10^{-10} T^4 + 1.17 \cdot 10^{-13} T^5$]
Electron-lattice coupling factor, g (W/m^{3}K)	$2.0 \cdot 10^{16}$ [51]
Density, ρ_{gold} (kg/m^3)	19,300
Enthalpy of fusion, ΔH_{fus} (kJ/kg)	64.0
Thermal conductivity, k_{gold} (W/mK)	320
Melting temperature, T_m (K)	1337
Water properties at standard conditions	
Density, ρ_w (kg/m^3)	1000
Specific heat, $c_{p,w}$ (kJ/kgK)	4.184
Thermal conductivity, k (W/mK)	0.61
Critical temperature, T_{cr} (K)	647
At the gold/water interface	
Thermal conductance, G (W/m^{2}K)	$105.0 \cdot 10^6$ [33]

Table 2

Gold nanoparticle properties for calculations of optical properties

	52 nm Spheres	94 nm Spheres	Oriented Parallel	Oriented Perpendicular	El-Sayed Nanorods
Model	Mie	Mie	ADDA	ADDA	ADDA
Irradiation wavelength, λ (nm)	400	400	756	756	800
Dimensions	R = 26 nm	R = 47 nm	L = 48 nm	L = 48 nm	L = 44 nm
Aspect ratio	1	1	3.4	3.4	4.1
Volume, V_p (nm^3)	73620	434900	6671	6671	3833
Refractive index[2]	1.2540 + 1.4751i	1.2494 + 1.4717i	0.2331 + 3.4785i	0.2331 + 3.4785i	0.2704 + 3.8249i
Absorption cross section, A_{abs} (nm^2)	3677	13570	5127	6.887	3771
Absorption efficiency[3]	1.731	1.956	11.85	0.0159	13.19

[1] The aspect ratio is defined as the tip-to-tip distance divided by the particle diameter.

[2] The refractive indices are corrected for surface damping for the particles in water (n = 1.333).

[3] The absorption efficiencies are computed by dividing the calculated absorption cross-sections by the geometric cross-section of a volume equivalent sphere.

J Phys D Appl Phys. Author manuscript; available in PMC 2011 July 26.